Supplementary Information for:

Ultra-small PbS nanocrystals as sensitizers for red-to-blue triplet-fusion upconversion

Christian J. Imperiale, Philippe B. Green, Minhal Hasham, Mark W.B. Wilson*

University of Toronto, Department of Chemistry, Toronto, ON, M5S 3H6

*mark.w.b.wilson@utoronto.ca

Table of Contents

Section 1: Materials and Methodology

Materials

Lead (II) oxide (99.999%), hexamethyldisilathiane (TMS-S), oleic acid (OA, 90%), 1-octadecene (ODE, 90%) and oleylamine (OLA, 70%) were all purchased from Sigma-Aldrich and used for synthesis as received. 9-bromoanthracene (94%), 4-ethoxycarbonylphenylboronic acid (>95%), palladium (0) tetrakis(triphenylphosphine) (99%), and potassium carbonate (90%) were purchased from Sigma-Aldrich and used for synthesis as received. Hydrochloric acid was purchased from Fisher and used as received. Diphenyl anthracene (DPA, 99.9%) was purchased from Alfa-Aesar and used for spectroscopy without further purification.

Synthetic Methodology

Synthesis of ultrasmall PbS nanocrystals. Small PbS nanocrystals were synthesized as previously described.[1] Using an adapted hot injection synthesis, $Pb(oleate)_2$ was synthesized *in situ* by cracking PbO (1 eq.) in a solution of OA (5 eq.), ODE and OLA (10 eq.) at 120°C. After reaching the desired temperature (60°C), a prepared solution of TMS-S (0.15 eq.) in ODE was swiftly injected and PbS nanocrystals were allowed to grow to completion. Subsequently, nanocrystals were sized using steady-state absorption spectroscopy and a sizing curve from our previous work,[1] and further studied via steady-state emission spectroscopy and time-resolved photoluminescence (TRPL). Nanocrystals were stored as a concentrated solution in tetrachloroethylene in a fridge (4°C) in a nitrogen glovebox.

Synthesis of EPA precursor. Ethoxycarbonylphenylanthracene (EPA) was synthesized similar to previous reports.[2] 9-bromoanthracene (1 eq.), $Pd(PPh_3)_4$ (0.05 eq.) and potassium carbonate (2 eq.) were added to a baked, 3-neck round bottom flask with 4-ethoxycarbonylphenylboronic acid (1.1 eq.). The flask was then set under N_2 and a 3:1:1 v/v/v solution of toluene, water and ethanol was added. The reaction solution was refluxed overnight and subsequently purified using a water/DCM extraction and silica gel chromatography.

Synthesis of CPA ligand. Carboxyphenylanthracene (CPA) was synthesized by adding purified EPA (1 eq.) to a 3-neck round bottom flask. The flask was then filled with a 1:1 v/v solution of THF and methanol, and while stirring vigorously, aqueous KOH (5 eq.) was added dropwise. The reaction mixture was then refluxed for 4 hours. Afterwards, aqueous HCl was added dropwise to the solution to yield a white precipitate, which was filtered and washed with a copious amount of water. ^{1}H NMR (400 MHz, $CDCl_3$, TMS internal standard): δ (ppm) = 7.36 (sext, 2H), 7.47 (sext, 2H), 7.54 (d, 2H), 7.60 (d, 2H), 8.06 (d, 2H), 8.28 (d, 2H), 8.53 (s, 1H) and 13.06 (br, 1H).

Ligand exchange of CPA-capped PbS nanocrystals. Native oleic-acid–capped PbS nanocrystals (150 μM) were added to a flask in a N_2-filled glovebox at room temperature, to which a solution of 5 mM CPA in anhydrous toluene was added. The ligand-exchange mixture was stirred gently for approximately 5 hours, after which the exchanged nanocrystals were precipitated 3 times with acetone and resuspended in toluene.

Preparation of Upconversion Samples

All upconversion samples were prepared in a N_2-filled glovebox with <5ppm O_2 levels. Samples were prepared with the identified concentration of PbS or PbS-CPA and DPA in toluene and sparged for approximately 1 min/mL solvent. All sample preparation and spectroscopy was performed at room temperature.

Steady-State Spectroscopy

Steady-state absorption spectra were acquired with a Perkin-Elmer Lambda 25 UV-Vis spectrometer. Steady-state emission spectra were taken with a home-built set-up at various excitation wavelengths. For upconversion studies excitation was at λ: 637 nm, using an externally driven (ThorLabs, LDC205C) laser diode (ThorLabs, HL63133DG). For direct excitation at λ: 405 nm, an integrated diode laser was used (ThorLabs, CPS405) was used. The emission set-up used an off-axis parabolic collimating mirror to direct collected fluorescence to a reflective optical fibre-coupler, which was then sent to an Ocean Optics Flame spectrometer. Absolute photoluminescence quantum yield (PLQY) measurements were obtained using an integrating sphere

(GigaHertz-Optik UPB-150-ARTA) coupled to an Ocean Optics Flame spectrometer, and PLQY values were calculated using the integrated emission intensity using the method of de Mello.[3]

Time-Resolved Spectroscopy

Time-resolved emission lifetime measurements of PbS QDs in solution were acquired using excitation from a λ: 470 nm pulsed diode laser (PicoQuant, LDH-D-C-470), and data was collected using a single photon avalanche diode (Micro Photon Devices, $PD-050-CTD) and PicoQuant HydraHarp 400 event timer. Time-resolved emission lifetime measurements of DPA were acquired using a λ: 375 nm pulsed diode laser (PicoQuant, LDH-D-C-375), and data was collected using the same detection scheme. The emission set-up used an off-axis parabolic collimating mirror to collect fluorescence, which was coupled through free space to the detector.

Photochemistry / Atom-Transfer Radical Polymerization (ATRP)

ATRP reactions were prepared and run as previously described by Ravetz et al.[4] Briefly, a vial of evaporated UC solution (originally containing [PbS-CPA]=4 μM, [DPA]=15 mM) equipped with a magnetic stir bar was resuspended in an equivalent volume of monomeric methyl methacrylate (1 eq.) in an N_2-filled glovebox ([O_2]<5ppm). To this solution, 0.05 eq. of ethylene glycol dimethacrylate gelling agent and 0.13 eq. of methyl α-bromophenyl acetate initiator were added. The vial was sealed with parafilm and covered with aluminum foil for transfer from the glovebox to the photochemical reactor. The vial was uncovered in the dark and subsequently stirred and irradiated at λ_{exc}= 637 nm (40 mW) for approximately 30 minutes.

Section 2: Derivation and Supplementary Discussion for Modelling

Steady-State Kinetic Model

We have previously described[5] the steady-state kinetic model used to derive Figure S8, however we review the fundamental equations here. Briefly, under continuous wave excitation of our UC system, we assume that steady-state populations of the relevant excited-state chromophores arise based on a few key transfer and decay pathways. Notably, we use both experimentally observed and literature values for these rate constants, and first assume irreversible TET and a triplet lifetime on ligands that is long compared to the characteristic times of transfer, though we will relax these assumptions in the dynamic below. We consider the rate equation for the concentration of triplet-excited free-floating annihilator molecules:

$$\frac{d[^3DPA^*]_t}{dt} = -k_{TF}[^3DPA^*]_t^2 - k_{Tdec,DPA}[^3DPA^*]_t + k_{TET2}[^3CPA^*]_t[DPA]_t$$

Where:

- $[^3DPA^*]_t$ is the instantaneous concentration of triplet-excited annihilators in solution
- $[DPA]_t$ is the instantaneous concentration of ground-state annihilators in solution
- $[DPA]_0 = [^3DPA^*]_t + [DPA]_t$ is the total concentration of free-floating annihilator in solution
- $[^3CPA^*]_t$ is the instantaneous concentration of triplet-excited ligands on the sensitizer surface
- k_{TF}, k_{Tdec}, k_{TET_2} are the rate constants of bimolecular triplet-fusion, monomolecular triplet decay and triplet energy transfer from the surface-bound ligands to the free-floating acceptors, respectively.

We also consider the generation of photoexcitations in the UC system by the rate equations for the hybrid, two-component triplet sensitizer, where we track the excited-state populations on the quantum dots $[^3QD^*]_t$ and the exciton extractor ligands $[^3CPA^*]_t$ separately, in anticipation of the dynamic model below.

$$\frac{d[QD^*]_t}{dt} = \Phi_{Laser}[QD_0 - QD^*]\sigma_{sens} - k_{QD}[QD^*]_t - k_{TET}[QD^*]_t[CPA]_t$$

$$\frac{d[^3CPA^*]_t}{dt} = k_{TET}[QD^*]_t[CPA]_t - k_{TET2}[^3CPA^*]_t[DPA]_t - k_{Tdec,CPA}[^3CPA^*]_t$$

Where:

- $[^3QD^*]_t$ is the instantaneous concentration of triplet-excited sensitizers (i.e. quantum dots) in solution
- $[QD]_0$ is the initial concentration of ground-state sensitizers in solution
- $[CPA]_t$ is the instantaneous concentration of ground-state ligands on the sensitizer surface
- Φ_{Laser} is the photon flux of the excitation laser
- σ_{sens} is the absorption cross-section of the quantum dot sensitizer
- k_{QD} is the reciprocal of the weighted-average excited state lifetime of the sensitizing QDs (See Figure S6, Table S2), and k_{TET} is the effective rate constant of triplet energy transfer from the QD to the surface bound ligands, and k_{Tdec_L} is the rate of monomolecular decay on the ligands.

From these steady-state kinetic equations, we calculate the UC brightness at a variety of laser excitation intensities and sensitizer excited-state lifetime (i.e. k_{QD}) to simulate the power dependence of UC emission, from which Figure S8 is generated.

Dynamic (Quasi-Equilibrium) Model

We employ a time-evolving kinetic model to more closely investigate the photoluminescence dynamics of PbS QDs in the presence/absence of triplet-accepting ligands and to clarify the consequences of TET, rTET and the presence of a secondary triplet acceptor in the system. This model parametrizes the nanocrystal emission and quenching as three subpopulations, each a two-state system with distinct, first-order dynamics, and was motivated by previous work on carboxylic acid ligand binding to CdS nanocrystals,[6] and exciton extraction in the widely studied CdSe/9-ACA hybrid sensitizer.[7] Briefly, our TRPL data from unexchanged PbS QDs shows a non-monoexponential decay that is effectively parametrized by a weighted triexponential fit (see Figure S6, Table S2). Thus, we consider that photoexcitation of the QD yields a fit-weighted initial population of emissive 'states,' each with a corresponding fitted monoexponential decay constant. Following photoexcitation, any of these states are available for transfer to a ground-state CPA ligand, and we assert that the rate of TET is equal for each sub-population, and for all QDs in the same subpopulation. Notably, we tracked the triplet-excited CPA populations separately for each of the three QD sub-populations, so that triplet-excited CPA ligand could only undergo rTET to QDs with the same dynamics. Other than this back-transfer, all ^{3}CPA* had identical decay pathways.

Though ligand loading would be expected to cause a dispersity of the TET rates within the ensemble (Figure S1), and a binomial binding model could be applied, we did not consider that our data would meaningfully constrain this choice. Then, we excluded bimolecular recombination channels occurring in the quantum dots or between excitations on the ligands because our transient photoluminescence experiments were performed in the low-excitation limit (consistent with the intensity-independent dynamics that we observe experimentally around our standard excitation flux; Figure S7). The lack of observed bimolecular decay processes other than triplet fusion between free-floating DPA molecules also supported our simplification to use an ensemble-averaged concentration of excitations on quantum dots and ligands, rather than propagating the discreet dynamics of a distribution functionalized quantum dots. Lastly, we asserted that all CPA excitations had a uniform transfer rate to free-floating DPA, and that this transfer was irreversible.

The differential equations used to solve the resulting initial value problem can be written as follows:

$$\frac{[QD_i^*]}{dt} = -\left(k_{QD_i} + k_{TET}\right)[QD_i^*] + k_{rTET}[{}^3CPA_i^*]$$

$$\frac{[{}^3CPA_i^*]}{dt} = -\left(k_{rTET} + k_{Tdec} + k_{TET2}\right)[{}^3CPA_i^*] + k_{TET}[QD_i^*]$$

$$\frac{[{}^3DPA_i^*]}{dt} = k_{TET2}[{}^3CPA_i^*]$$

Where k_{QD_i} is the rate constant of photoluminescence decay of the ith sub-population of photoexcited QDs, k_{TET} is the characteristic rate constant of TET from QD to CPA, k_{TET2} is the rate constant of TET from CPA to free-floating DPA, k_{Tdec} is the rate constant of monomolecular decay of CPA, and k_{rTET} is the rate constant of reverse TET. As a result, $K \equiv \frac{k_{TET}}{k_{rTET}}$. When tracking concentrations, *i*=1, 2 or 3 denotes the correspondence to one photoexcited subpopulation of QDs/CPA/DPA. Our model considered instantaneous/impulsive excitation, because the laser pulse duration (~100ps) was much shorter than the shortest lifetime for any subsequent process (i.e. $k_{QD_1} \sim 370ns$). Following numerical propagation of the three sub-population equations, the instantaneous contributions from each sub-populations for each state are summed at each time-point to generate ensemble population dynamics, such as are shown in Figure 3. Lastly, the decay-constant–scaled population was time-integrated to calculate the branching ratios of photoexcitation decay.

Section 3: Supplementary Figures

3.1 Estimation of QD ligand loading

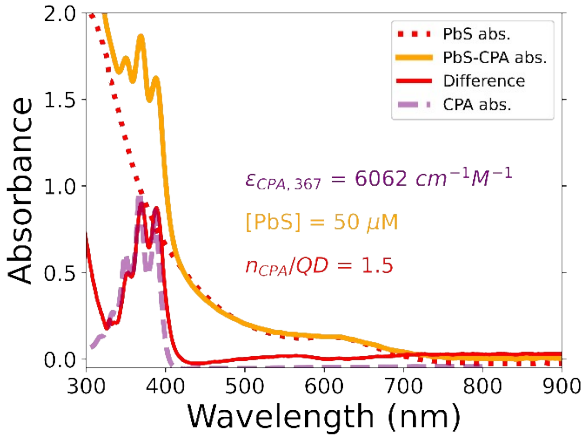

Figure S1. UV-Vis absorbance spectra of PbS, CPA-functionalized PbS, and free CPA. The molar absorption coefficient of free-floating CPA at λ: 367 nm ($\varepsilon_{367,CPA}$) was measured via steady-state absorption spectroscopy (violet curve). The concentration PbS QDs was determined using the methods described by Moreels et al.[8] The raw difference between the PbS and PbS-CPA spectra is included (solid red curve), representative of the upper bound on the concentration of coordinated CPA ligands. Then, using the previously determined $\varepsilon_{367,CPA}$, the concentration of bound CPA ligands ($\langle n \rangle$=1.5) was calculated from the difference spectrum. We observe a minor red-shift of the CPA absorption peaks after functionalization (< 3nm).

This relatively low ligand-loading primarily arises from the instability to ripening that we observed when subjecting these ultra-small QDs to X-for-X ligand exchange procedures with elevated ligand concentrations. Instability to ripening at high ligand concentrations arises due to mass action,[9] and ultra-small particles are especially vulnerable.[1] Particularly, noting our recent demonstration of the selectivity on larger PbS QDs for the sterically unencumbered and labile binding sites at facet-edges of a similar ligand exchange using a comparable anthracene ligand (9-ACA, which does not does not include the phenyl spacer found in CPA),[10] this could indicate that surface reconstruction in response to altered surface stoichiometry may promote mass-transfer and ripening. However, further studies are necessary to establish the presence and nature of any facet-dependence of X-X ligand exchange procedures in ultra-small PbS QDs.

3.2 Consideration of FRET backtransfer and far-field re-absorption

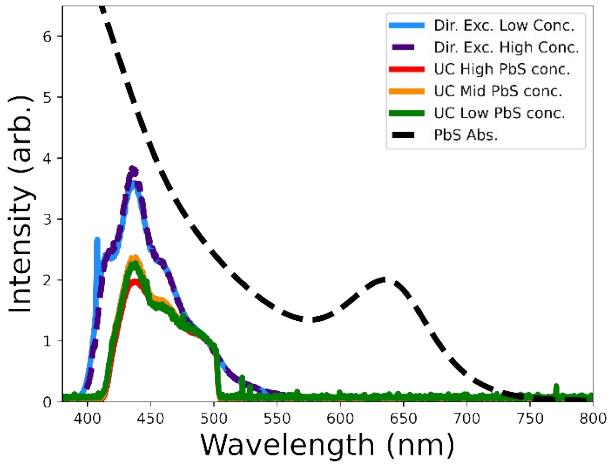

Figure S2. Steady-state PbS absorption (dashed black line), direct-excitation PL from solutions of DPA only (dilute (solid blue) and concentrated (dashed purple)) solutions, and upconverted emission from mixed solutions of DPA and CPA-functionalized ultra-small PbS following excitation of the QD sensitizers at λ: 637nm (red, orange, green). All emission spectra are normalized to the longest wavelength vibronic feature (λ_{em}=490nm).
The bluest DPA emission features (i.e. 0-0, 0-1 vibronic transitions) are suppressed in all samples with QDs ([DPA]=15 mM in all three traces, red [PbS-CPA]= 15 μM, orange [PbS-CPA]= 4 μM and green [PbS-CPA]= 1.5 μM; QD concentrations chosen to span the range able to achieve adequate triplet sensitization), and we observe a slight dependence of the relative strength of the residual 0-1 feature in the upconverted emission on the concentration of the PbS QDs. Together with Figure S3 (below), the spectral filtering is consistent with far-field reabsorption by QDs, rather than FRET.
Inspection of the direct excitation (λ_{exc}=405nm) emission of dilute (1 mM) and concentrated DPA (15 mM) provides evidence that the concentration of ground-state DPA in solution is not primarily responsible for the change in the emission spectrum via aggregation or self-absorption.

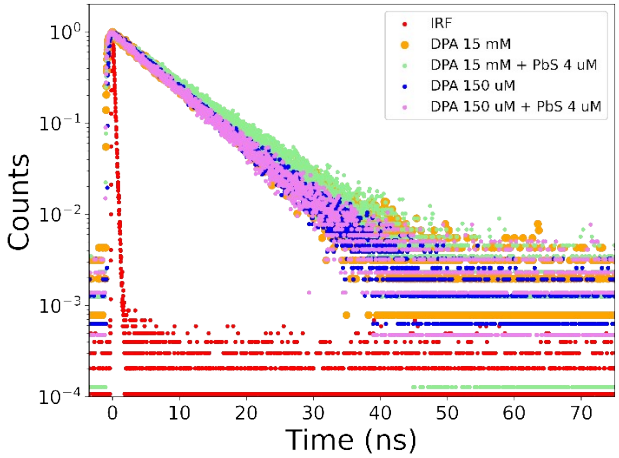

Figure S3. Time-resolved photoluminescence (TRPL) trace of DPA emission. PL dynamics of neat DPA in solution are unchanged across two orders of magnitude of concentration (orange circles, 15 mM; blue circles, 150 μM). The points in the high concentration DPA-only trace (orange circles) are enlarged for clarity. Introducing PbS-CPA at concentrations required for UC (4 μM) shows no change in lifetime at low DPA concentrations (violet circles), and only a marginal extension of DPA emission lifetime at higher DPA concentrations (green circles). This data, in addition to Figure S2, leads us to conclude that any suppression of the bluest edge of DPA UC emission arises from far-field reabsorption by ground-state PbS QDs, and not parasitic FRET.

3.3 Steady-state QD photophysics

Table S1. Steady-State photoluminescence quantum yield (PLQY) of PbS nanocrystals

	$\lambda_{excitation}$	PLQY (%)
PbS-OA	637	6.7
PbS-CPA	637	5.4
PbS-CPA	532	5.8
PbS-CPA w/ DPA (15 mM)	637	5.8

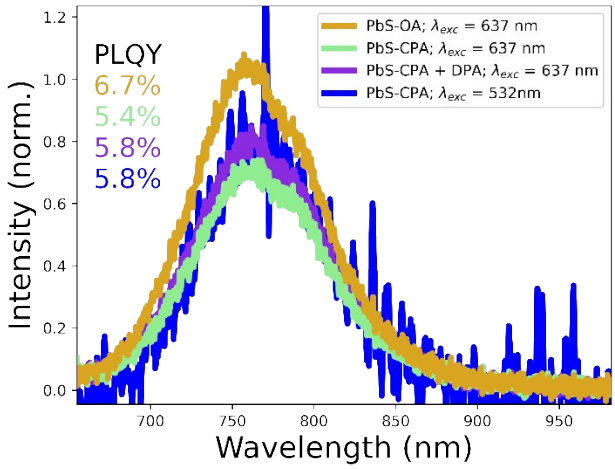

Figure S4. Steady-state photoluminescence quenching of ultra-small PbS QDs. Photoluminescence spectra are obtained from QDs with native OA ligands, and compared to CPA-functionalized QDs with and without free-floating DPA as a secondary energy outlet, and with either band-edge or 'hot' photoexcitation. The consistent lineshape of the steady-state PL traces provides preliminary evidence that the entirety of the QD distribution is quenched homogeneously (See Figure 4). Absolute PLQYs from each system are determined using an integrating sphere as described above, and this value is used to scale the integrated area of spectra relative to the OA-capped control, which is normalized. These values are used to determine the total quenching efficiency, which is compared to the time-integrated predictions from the kinetic model (Fig 3.)

3.4 Atom-transfer radical polymerization and control experiments

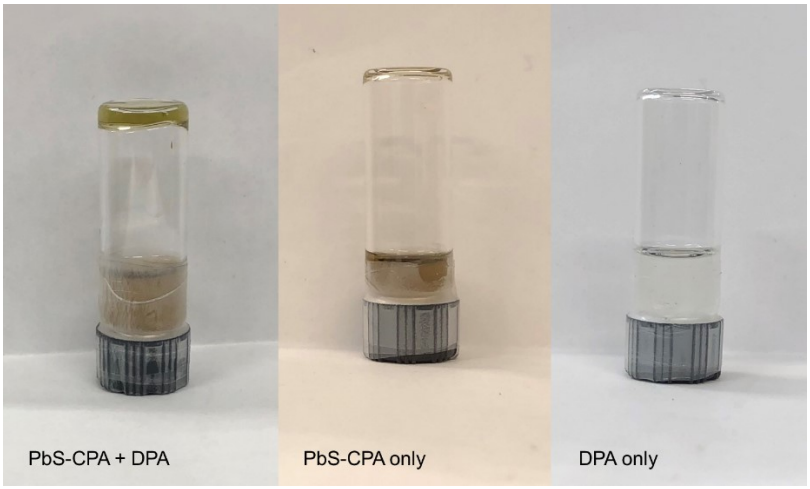

Figure S5. Photographic results from UC-mediated ATRP reactions. All samples were prepared in the glovebox and kept covered until exposed to excitation at λ: 637nm. When removing either the triplet sensitizer (PbS-CPA) or the emitter (DPA) upconversion is prevented, and thus polymerization/gelation do not proceed.

3.5 Three-Parameter Fit and Supplementary TRPL Data

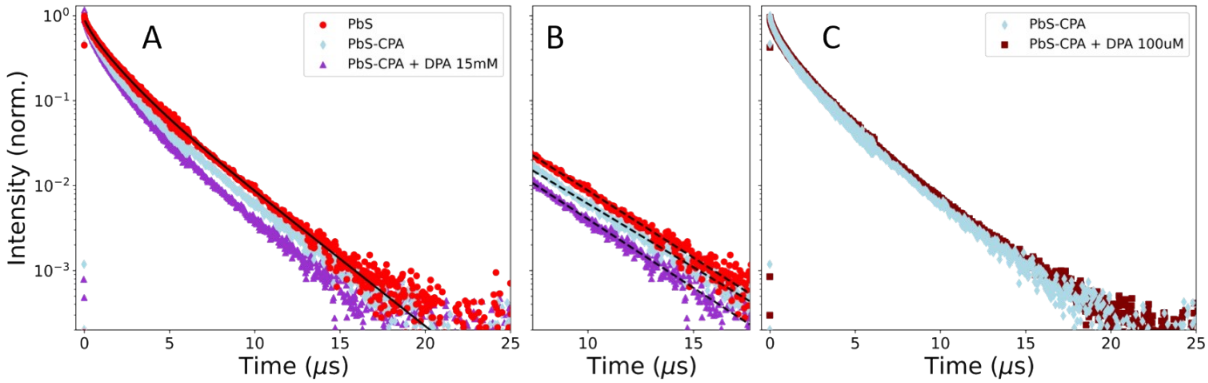

Figure S6. TRPL of PbS nanocrystals under various quenching conditions. The red circle, coral diamond, and violet triangle traces are the same as those presented in the main text. A) Full TRPL data. Compared to Figure 3, the unfunctionalized PbS trace (red circles) is brought to the front to highlight the suitability of the triexponential parametrization to these emission dynamics. We use the lifetime and weighting components of the tri-exponential fit for our equilibrium model as described above (See Table S2 for fitted parameters and weighted-average lifetime, and Figure S10 for further discussion of the parametrization).
B) Expanded view of long-time (t > 7 μs) emission highlighting differences of fitted monoexponential lifetimes based on the quasi-equilibria established by quenching and excitation recycling pathways. Qualitatively, the PL decay of CPA-functionalized QDs in this time-regime is slowed by exciton back-transfer relative to either unfunctionalized QDs, or PbS-CPA samples in solution with DPA as a secondary triplet acceptor. Monoexponential lifetimes fitted exclusively to this long-time window are in Table S3.
C) TRPL data taken with a low concentration (100 μM) of DPA (maroon squares). This shows dynamics comparable to the PbS-CPA trace without any DPA (light blue diamonds), though with a slight, perceptible deceleration in the decay. Analogous behaviour has been noted previously by Piland et al. studying CdSe quenching with anthracene carboxylic acid ligands in the presence of free-floating DPA.[7] There, the authors note that increasing the free-floating DPA concentration slightly reduces the concentration of bound acene extractor ligands due to a cooperative solubility effect between the acene molecules, though this effect saturates at high DPA concentrations. Thus, we conclude that 100 μM, we may have a decreased average number of surface-bound CPA ligands under those conditions, while the increased quenching at 15 mM DPA arises from the enormous excess of DPA driving transfer forward, as well as some possible direct transfer, as discussed in the main text.

Table S2. Fit parameters from triexponential fit of unfunctionalized PbS nanocrystals.

i	α_i	τ_i (μs)
1	0.16	0.37
2	0.40	1.33
3	0.34	2.78

Table S3. Time-resolved lifetimes of PbS nanocrystals under various quenching conditions. $\bar{\tau}_{emission}$ is the weighted average lifetime of the traces above (Fig. S6A), based on a triexponential parametrization. We include the lifetime components extracted for the fit of native PbS QDs, as these were central to our three-state parameterization. Uncertainty values are the standard deviations calculated from long-time monoexponential fits.

	$\bar{\tau}_{emission}$ (μs)	$\tau_{long\ time}$ (μs)	% Change ($\tau_{long\ time}$)
PbS-OA	2.13	2.65 ±0.04	--
PbS-CPA	1.96	2.72 ±0.04	+2.6
PbS-CPA w/ DPA (100 μM)	2.04	2.62 ±0.02	-1.1

PbS-CPA w/ DPA (15 mM)	1.54	2.38 ±0.05	-10.2

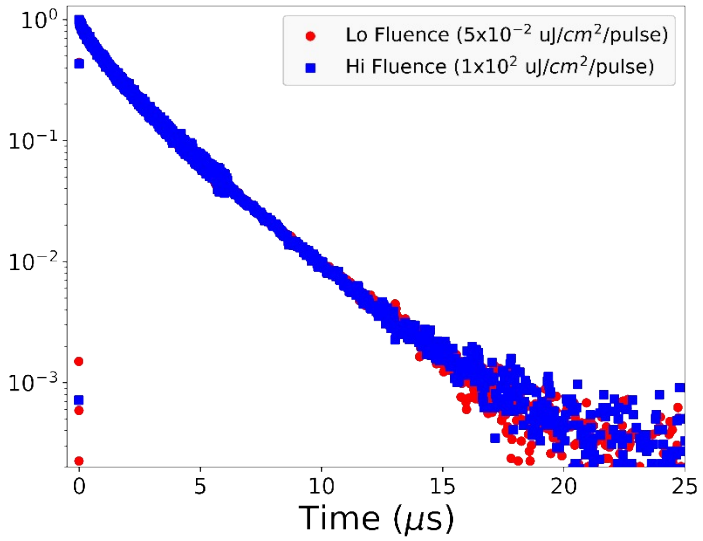

Figure S7. Power-dependent TRPL traces of PbS-OA solutions. No significant acceleration of dynamics due to bimolecular recombination processes on isolated QDs in solution are observed, as expected at these fluences. Thus, TRPL results reported in this work were measured at the higher fluence (100 μJ/cm^2/pulse) to accelerate data collection. This data also supports the exclusion of bimolecular recombination channels for excitations on QDs or the CPA ligands from our kinetic model, as discussed above.

3.6 Results from Steady-state (Irreversible Transfer) Kinetic Model

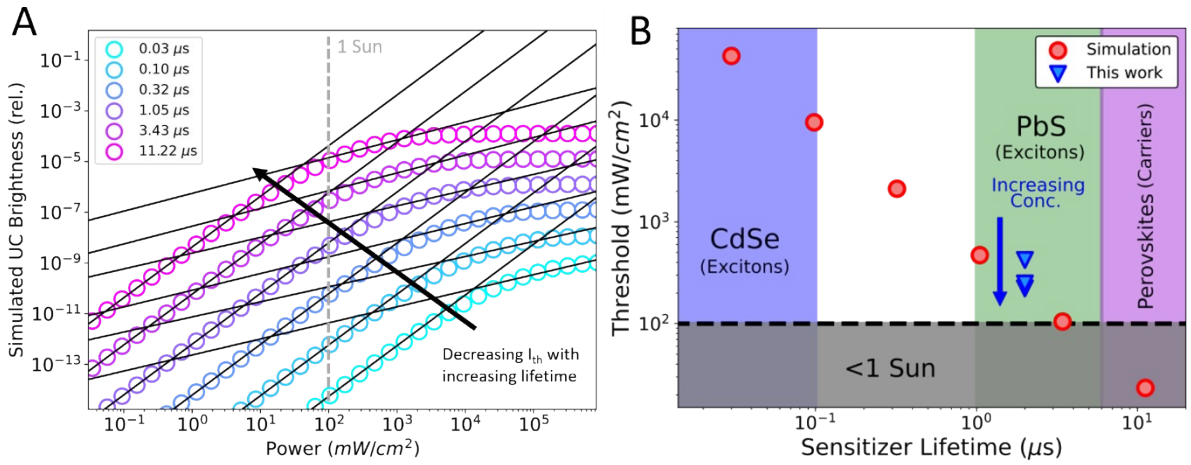

Figure S8. A) Simulated UC power dependence measurement with varying sensitizer lifetimes using the irreversible transfer model (See section 2). Other than the QD lifetime, all other rate constants of transfer and decay are kept constant (parameters are given in Table S4 below). We use the experimentally-observed value of k_{TET} , and literature values for DPA photophysics. However, unlike our observations, this simplified model assumes irreversible transfer and a long triplet lifetime on ligands, so the results are qualitative only.

B) Simulated max-efficiency thresholds with respect to sensitizer excited-state lifetime. Experimental results from this work (blue triangles) are included. Regions corresponding to the characteristic lifetimes of other inorganic sensitizers are coloured, though this comparison is simplistic as the other simulation parameters are not changed. Increased sensitizer excited-state lifetime yields greater triplet 'injection' into the acceptor population at steady-state due to excited-state partitioning based on weighted transfer and decay constants. However, our subsequent analysis considers equilibrium excited-state partitioning, given that this (along with a significant reduction in the triplet lifetime on bound transmitter ligands) is required to explain our TRPL data. Speaking qualitatively, the inclusion of a parasitic back-transfer channel would decrease the concentration of triplet-excited acceptors compared to this simplified model, monotonically shifting the calculated value of the thresholds to higher intensities. Thus, the intuition that max-efficiency threshold decreases monotonically with sensitizer lifetime holds. However, further quantification of this non-linear effect would benefit from additional experimental constraints on e.g. the transfer dynamics between the transmitter ligands and the DPA, as well as experiments with the other sensitizer material systems in question, and so is left for future work. Indeed, the alignment between the observed threshold intensities in our system and those calculated in the simple model arises in part because of the co-incidental similarity of the average lifetime of excitations on the QD to those of spin-triplet excitons on the CPA ligands.

Table S4. Parameters used to simulate steady-state upconversion power dependence, and lifetime-dependent thresholds.

[QD] (μM)	n_{CPA} ($[CPA]_0$) (μM)	σ_{sens} (s^{-1} cm^{-2})	$k_{TET,CPA}$ (s^{-1})	$k_{Tdec,CPA}$ (s^{-1})	$[DPA]_0$ (mM)	$k_{TET,DPA}$ (s^{-1})	$k_{Tdec,CPA}$ (s^{-1})	k_{TF} (M^{-1} s^{-1})
15	2 (30)	$3x10^{-16}$	$1.8x10^{5}$	$1x10^{3}$	15	$1x10^{8}$	$1x10^{3}$	$2x10^{-7}$

3.7 Supplementary TRPL and (Dynamic) Kinetic Modelling Data

Table S5. Kinetic parameters used to calculate TRPL/population model (Figure 3, main text).

	k_{rad1}, k_{rad2}, k_{rad3} (μs^{-1})	$\alpha_1, \alpha_2, \alpha_3$	k_{Tdec} (μs^{-1})	k_{TET} (μs^{-1})	k_{TET2} (μs^{-1})	K_c (k_{TET}/k_{rTET})
PbS-OA	2.7, 0.75, 0.36	0.16, 0.40, 0.34	0.32	--	--	--
PbS-CPA	2.7, 0.75, 0.36	0.16, 0.40, 0.34	0.32	0.18	--	0.66
PbS-CPA w/ DPA (15 mM)	2.7, 0.75, 0.36	0.16, 0.40, 0.34	0.32	0.18	0.67	0.66

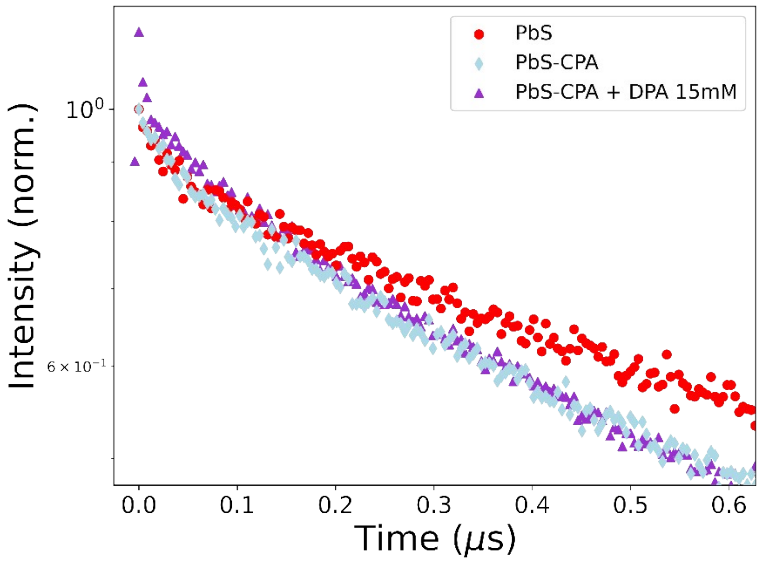

Figure S9. Expanded view of early time TRPL data presented in main text Figure 3B. As described in the main text, red and blue traces are normalized to t=0, and the purple trace is normalized to the blue trace at 150ns to permit fair comparison of the relative PL intensities at all later times. The processes giving rise to the rapid, parasitic emission at times <100ns (purple triangles, above) are not considered in the construction of our equilibrium model.

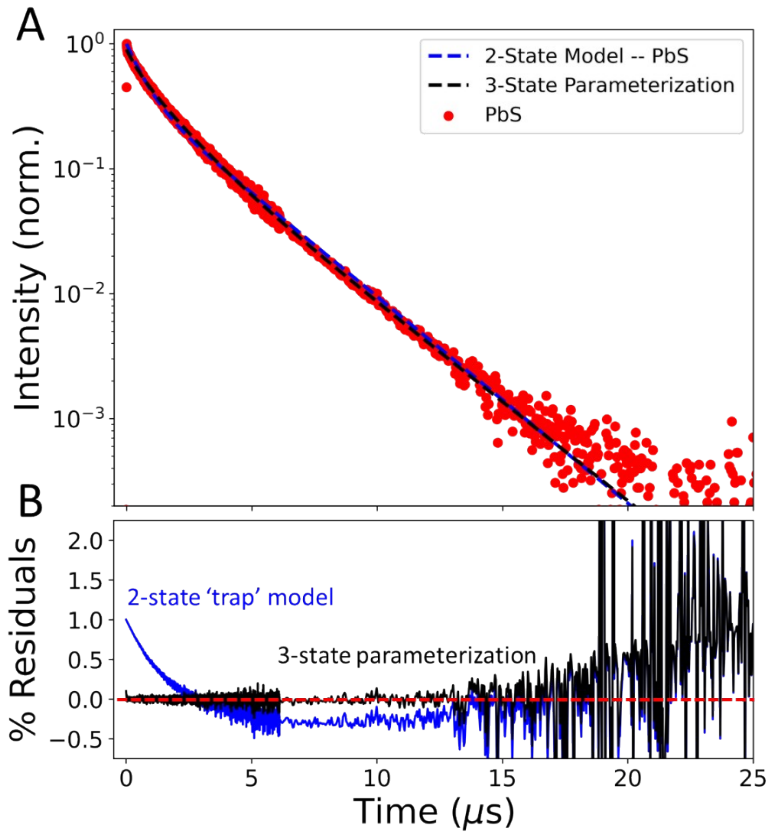

Figure S10. Comparison of the chosen parameterized 3-population model to an alternate 'trap' model to describe multiexponential decay of as-synthesized QDs. As described above, the parametrized model takes the lifetimes values weighted by the prefactors extracted from the triexponential fit (See Table S2). Data beyond 20us is dominated by noise.

We also considered a model where a uniform ensemble of (emissive) two-level systems (with lifetimes equal to that of the weighted average QD lifetime) are each in dynamic equilibrium with a uniform non-emissive 'trap'. This additional 'trap' may accept photoexcitations from the emissive band-edge exciton (trapping), transfer population back to the band-edge exciton (de-trapping), and itself undergo population decay, and we asserted that each process had a characteristic first-order rate.

However, when fitting this model to the data, we found that the best-fit rate constants of trapping/de-trapping (μs timescale) were poorly matched with experimental observations of single-carrier trapping in PbS QDs,[11,12] and even rough agreement with the data required the trap decay to have a similar lifetime to the band-edge decay, which is inconsistent with reports from targeted experiments in other QD materials.[13] These physical considerations, along with the superior agreement between the parametrized model and the experimental data led us to use the 3-population parameterization for our kinetic modelling. The applicability of this model was reinforced by the good agreement between steady-state observables and time-integrated modelled quantities (Table S6, S7).

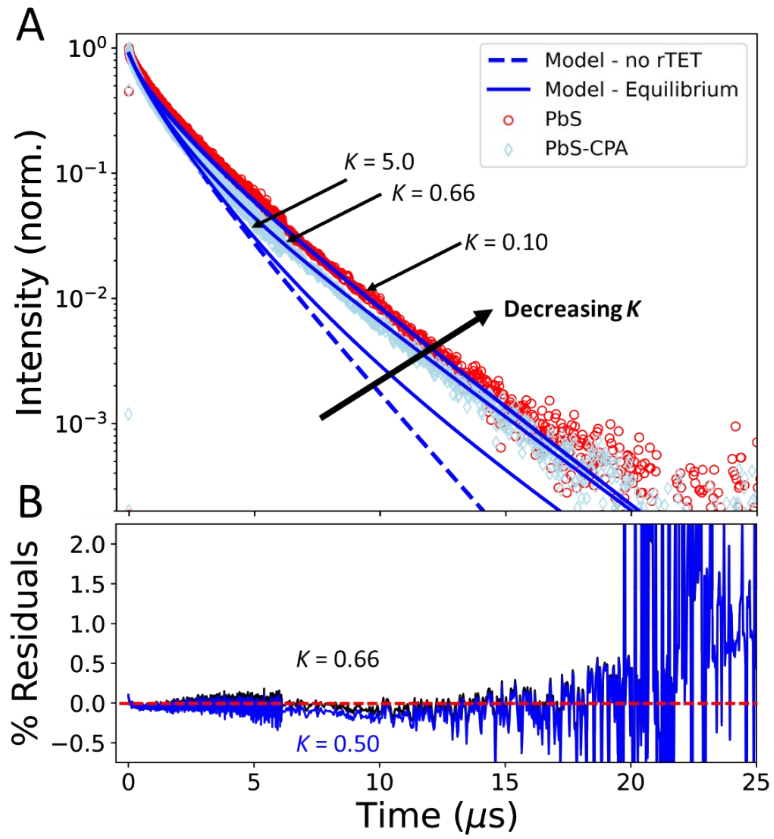

Figure S11. Comparison of simulated population dynamics under the assumption of irreversible transfer, compared to equilibrium dynamics with varying equilibrium constants (*K*). Solid blue lines show the effect of varying K (i.e. forward/reverse bias of the equilibrium between QDs and CPA ligands), while holding the rate constant for forward TET rate at the same value to simplify comparison. The residual trace (B) shows that even small changes in *K* lead to observably worse fits to experimental data, particular in the regime around 10us when equilibrium dynamics dominate. Data beyond 20us is dominated by noise.

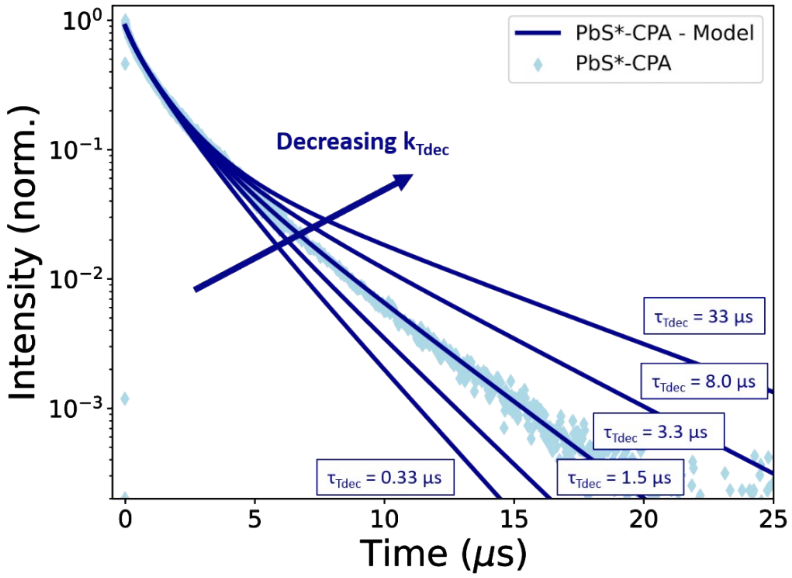

Figure S12. Comparison of simulated PbS population dynamics with various ^{3}CPA* monomolecular decay constants. Lengthening the lifetime of ^{3}CPA* (decreasing k_{Tdec}) yields increased reverse triplet energy transfer, and an enhanced 'delayed photoluminescence' effect in PbS QDs.

An intriguing result of this equilibrium modelling is that the lifetime of ^{3}CPA* bound to the NC surface appears to be significantly reduced from the millisecond-scale phosphorescence dynamics reported for free-floating anthracene derivatives in de-aerated solutions.[14] Under these equilibrium conditions, if the ^{3}CPA* lifetime were comparable to that of free-floating CPA in solution, we would expect to observe a large, delayed-photoluminescence tail in the TRPL of the PbS QDs.

3.8 Branching Ratio Calculations

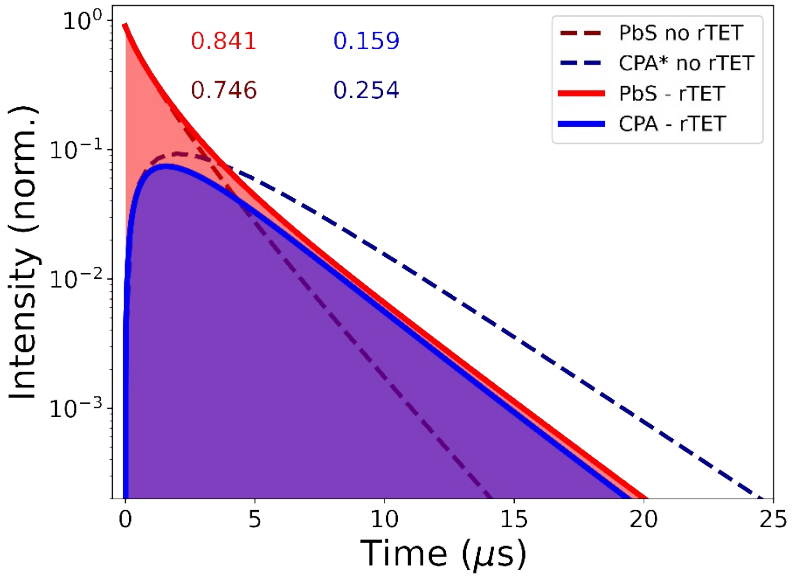

Figure S13. Investigation on the role of rTET in the PbS-CPA model. Removing the rTET channel (i.e. assuming no equilibrium excited-state dynamics) yields an increased fraction of incident excitations that decay via ^{3}CPA*. In the complete upconversion system, suppressing rTET would increase the fraction of excitations that end up on the final acceptor. However, parallel improvements to the branching ratio between TET and decay on the QD, and efforts to lengthen the lifetime of triplets on the CPA, would also be essential for maximum performance

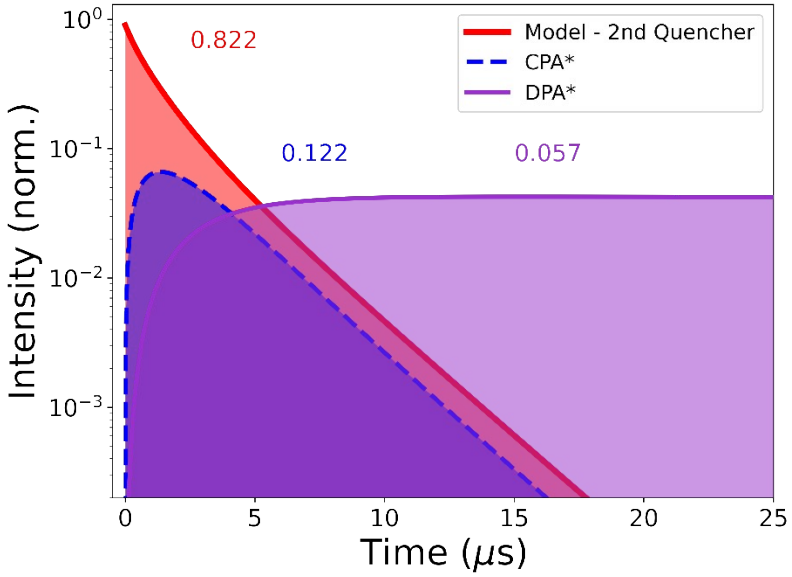

Figure S14. Comparison of excitation decay outlets in the complete PbS-CPA + DPA model with best-fit experimental parameters. The annotated branching fractions are obtained by calculating the decay-constant–weighted time-integral of the excited state population. Only a small percentage (5.7%) of photoexcitations end up reaching the final acceptor (DPA)

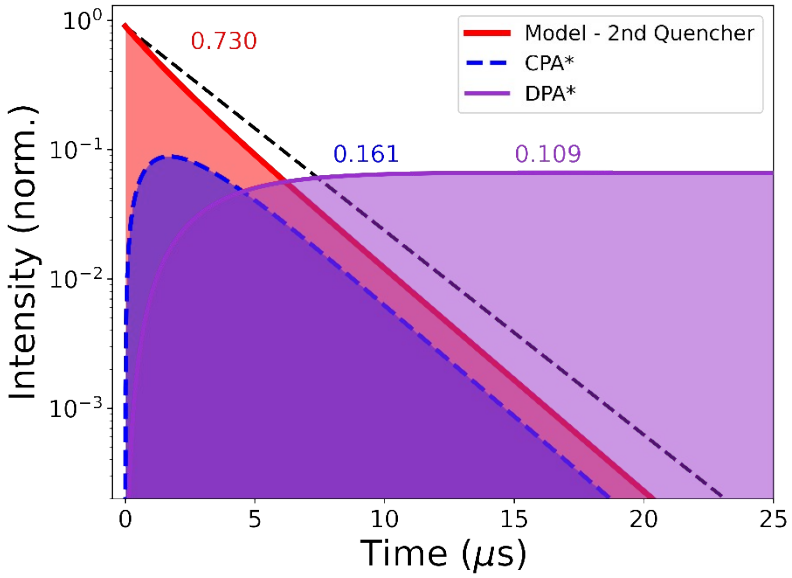

Figure S15. Comparison of excitation decay outlets a hypothetical QD-CPA + DPA system, where the entire QD population decays with a time constant equal to that of the longest observed from our triexponential fit (2.7 μs, dashed black line), reflecting a plausible 'best-case' scenario for advances in colloidal synthesis of this core-only material. The red trace displays the QD population decay in the presence of CPA and DPA, the blue dashed trace is the population decay of triplet-excited CPA ligands, and the purple trace is the population dynamics of triplet-excited DPA. Though the ultimate yield of triplets to the DPA is doubled compared to the present realization (Figure S14), the majority of excitations still recombine on the QDs in this endothermic system given the QD lifetime, and monomolecular triplet decay on the ligands remains a significant loss channel.

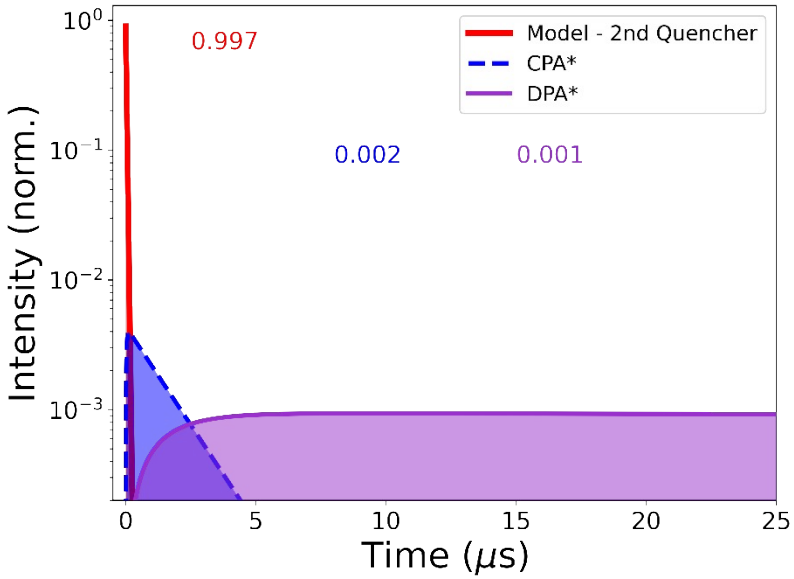

Figure S16. Comparison of excitation decay outlets a hypothetical QD-CPA + DPA system, where the entire QD population is assumed to decay with a time constant equal to 30 ns (dashed black line, under red trace). The red trace displays the QD population decay in the presence of CPA and DPA, the blue dashed trace is the population decay of triplet-excited CPA ligands, and the purple trace is the population dynamics of triplet-excited DPA.

Table S6. Total branching decay ratios calculated from decay-weighted time-integration of the excited-state populations, assuming 100% of photoexcitations begin on PbS QD. These values annotate Figures S13 and S14.

	Excitations that decay on QD	Excitations that decay on CPA	Excitations that reach DPA
PbS	1.0	--	--
PbS-CPA	0.841	0.159	--
PbS-CPA + DPA	0.822	0.122	0.057

Table S7. Branching decay ratios of ^{3}CPA* excitations considering excitation recycling via rTET. Calculations are based on the time-integrated branching ratios in Table S6 and additional decay-weighted time-integrations of the numerical model (Figure S13, S14), each scaled to f_{CPA}: the fraction of photoexcitations that reach CPA at least once in the full system (PbS-CPA+DPA). We can determine the numeric value $f_{CPA} = 0.254$ because (given the assumptions in our model) it is equivalent to the fraction of excitations that decay on CPA in the absence of either rTET or a DPA quencher (Figure S13). For comparison, we also include the instantaneous decay fractions of each excited state from first-order kinetics. Because these calculations do not consider excitation recycling, they underestimate the fraction of excitations that decay on the CPA ligand, and overestimate the fraction that decay on the QD. These results highlight the parasitic nature of the faster-than-expected CPA monomolecular decay.

	CPA excitations that ultimately decay on the QD following rTET	CPA excitations that ultimately decay on CPA	CPA excitations that reach DPA
PbS-CPA	0.374	0.626	--
f_i/f_{CPA}	(0.841-0.746)/0.254	(0.159)/0.254	--
$\frac{k_i}{k_{rTET} + k_{Tdec}}$	0.443	0.557	--
PbS-CPA + DPA	0.299	0.480	0.224
f_i/f_{CPA}	(0.822-0.746)/0.254	(0.122)/0.254	(0.057)/0.254
$\frac{k_i}{k_{rTET} + k_{Tdec} + k_{TET2}}$	0.346	0.435	0.219

Table S8. Photophysical parameters of PbS relevant to UC.

	QD PLQY (%)	$\bar{\tau}_{emission}$ (μs)	Φ_{TET} (%)	$\tau_{transfer}$ (μs)	UC PLQE (w/ DPA; %)
PbS	6.7	2.13	--	--	<0.01[a]
PbS-CPA	5.4	1.96	19.4	5.4	Calc. IQE[b]: 1.0 Measured QE: 0.6

[a]UC emission was observed, but measured PLQY was below error threshold. [b]Maximum possible efficiency of this system based on the percentage of initial photoexcitations that reach DPA (Table S4) and the record UCQE from QD-sensitized upconversion in DPA.[15]

3.9 Additional Results from Wavelength-resolved TRPL Spectroscopy

Figures S17-S22 TRPL spectroscopy of PbS and PbS-CPA QDs probed within various spectral regions.

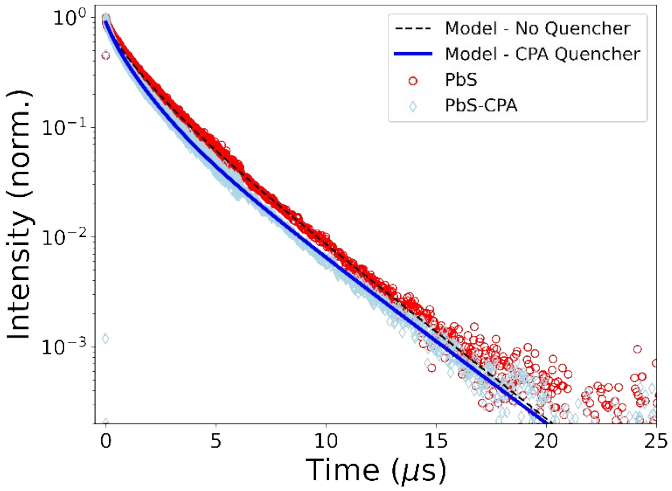

Figure S17. TRPL traces of PbS (red circles) and PbS-CPA (pale blue diamonds) QDs integrated over the entire PbS emission spectrum, compared with our equilibrium model (solid blue line).

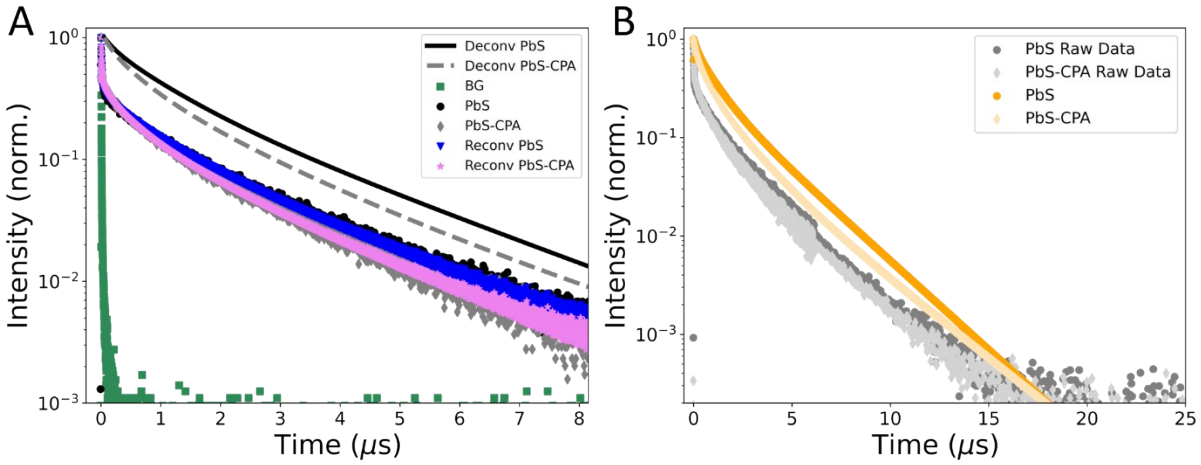

Figure S18. A) Deconvolution of background signal from TRPL trace for the shortest-wavelength spectral window. Raw experimental data measured from a cuvette filled with toluene only (green squares) shows the dynamics of a parasitic background signal that is relevant at these wavelengths. The raw data measured at these wavelengths from solutions of PbS only (black circles) or functionalized PbS (gray diamonds) includes a prominent contribution from this signal at very early times (t<50ns) due to the low count rate from PbS QDs in this spectral region relative to the background. (See Figure 4B for steady-state spectra)
Iterative reconvolution is used to isolate the emission dynamics of the two QD samples, and the bet fits of a triexponential parametrization are presented with solid black (PbS) and dashed grey (PbS-CPA) lines. As a qualitative check, the extracted triexponential dynamics are reconvoluted with the measured background signal to yield the blue triangle and pink star curves, which are in good agreement with the raw data. B) Deconvoluted TRPL trace over the full time range (orange circles and yellow diamonds), compared to the raw data (grey circles and light grey diamonds left in background) . After the rapid decay of the parasitic emission, the relative dynamics track qualitatively over the entire experimental range.

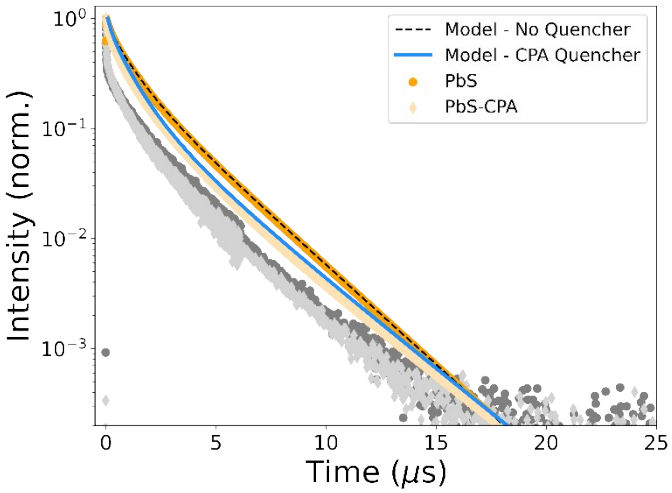

Figure S19. Deconvoluted TRPL traces of PbS (gold circles) and PbS-CPA (pale yellow diamonds) QDs in the region λ<700nm, compared with our equilibrium model. The raw data are presented in grey for reference (See FigS18 above).

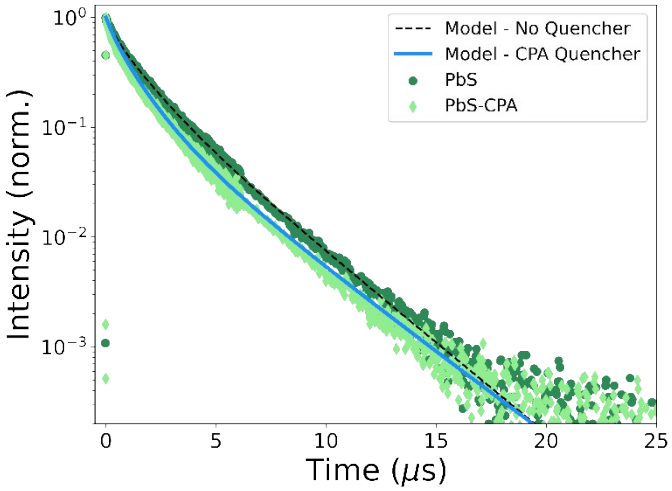

Figure S20. TRPL traces of PbS (dark green circles) and PbS-CPA (light green diamonds) QDs from 700nm<λ<750nm, compared with our equilibrium model.

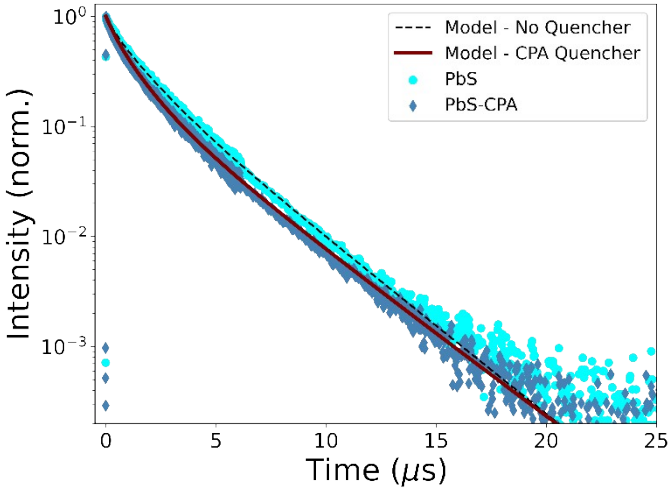

Figure S21. TRPL traces of PbS (cyan circles) and PbS-CPA (grey blue diamonds) QDs from 750nm<λ<800nm, compared with our equilibrium model.

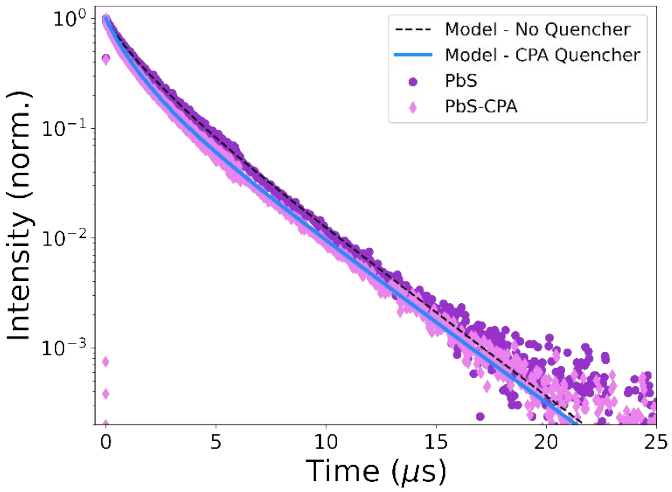

Figure S22. TRPL traces of PbS (violet circles) and PbS-CPA (light purple diamonds) QDs from 800nm<λ<900nm, compared with our equilibrium model.

Table S9. Parameters used to generate results from equilibrium model in Figures S17-S22. The QD decay constants are parameterized based on a triexponential fit of the native PbS dynamics in each spectral region, as described in Section 2.

Spectral Range	k_{QD1}, k_{QD2}, k_{QD3} (μs^{-1})	k_{Tdec} (μs^{-1})	k_{TET} (μs^{-1})	k_{TET2} (μs^{-1})	K_c (k_{TET}/k_{rTET})
Full Spectrum	2.7, 0.76, 0.36	0.32	0.18	--	0.66
λ < 700 nm	2.4, 0.91, 0.42	0.32	0.18	--	0.80
700 nm < λ < 750 nm	2.8, 0.79, 0.38	0.32	0.18	--	0.95
750 nm < λ < 800 nm	2.7, 0.78, 0.37	0.32	0.18	--	0.65
800 nm < λ < 900 nm	2.4, 0.72, 0.35	0.32	0.18	--	0.55

Table S10. Fitted emission dynamics of PbS nanocrystals under various spectral regions. Data from Figures S17-S22. Note that these lifetimes are calculated from a triexponential fit, and not from our equilibrium model. While the weighted average fitted lifetimes ($\bar{\tau}_{emission}$) of unfunctionalized PbS QDs lengthen slightly in lower energy ('redder') spectral regions, the reduction in average lifetime between unfunctionalized and functionalized QDs remains constant.

Spectral Range	$\bar{\tau}_{emission}$ (μs) PbS-OA	$\bar{\tau}_{emission}$ (μs) PbS-CPA	% Reduction
Full Spectrum	2.13	1.96	8.0
$\lambda < 700$ nm	1.85	1.67	9.7
700 nm $< \lambda <$ 750 nm	2.00	1.78	11.0
750 nm $< \lambda <$ 800 nm	2.14	1.96	8.9
800 nm $< \lambda <$ 900 nm	2.27	2.13	6.2

3.10 Size series and commentary on ultrasmall QD photophysics

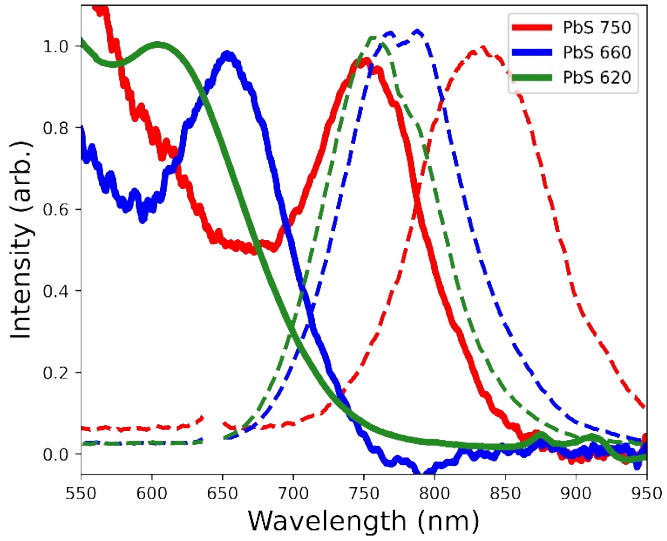

Figure S23. PbS QD size series: steady-state absorption (solid lines) and emission (dashed lines) of PbS QDs. The QDs employed for upconversion and sensitized photochemistry are presented in green (λ_{abs}=620nm, 2.0 eV; λ_{em}=760nm, 1.63 eV). Slightly larger QDs ($ø_{est}$=2.2nm) display slightly redder excitonic absorption feature (solid blue line; λ_{abs}=660nm, 1.88 eV) but only a minor shift in peak emission wavelength (dashed blue line; λ_{em}=775nm, 1.60 eV). Still larger QDs with a lowest energy absorption feature (solid red line; λ_{abs}=750nm, 1.65 eV) aligning with the peak emission of the ultrasmall QDs employed for upconversion are included for comparison. As discussed in the main text, the chemical/energetic potential of these QDs is bounded by the absorption and emission features, and so we use the simple average of these values as an estimate in our discussion.

Tables S11. Analysis of absorption and emission features presented in Figure S23, using the simple average between the two energies as an estimate of the energetic potential of ultrasmall PbS QDs, along with QD PLQY. The expected energy difference ($\Delta E_{expected}$) between the sensitizing QD and molecular triplet is calculated from the peak energy of the steady-state QD emission spectra. The calculated energy difference ($\Delta E_{calculated}$) between the sensitizing QD and molecular triplet is extrapolated from the measured equilibrium constants.

QD	E_{abs} (eV) (λ_{abs})	E_{em} (eV) (λ_{em})	$\Delta E_{expected}$ (meV)	$\Delta E_{calculated}$ (meV)	E_{av} (eV)	PLQY (%)
PbS 620	2.00 (620 nm)	1.63 (760 nm)	170	12.9	1.82	6.7
PbS 660	1.88 (660 nm)	1.60 (775 nm)	200	30.8	1.74	8.9
PbS 750	1.65 (750 nm)	1.46 (850 nm)	340	59.1	1.56	10.6

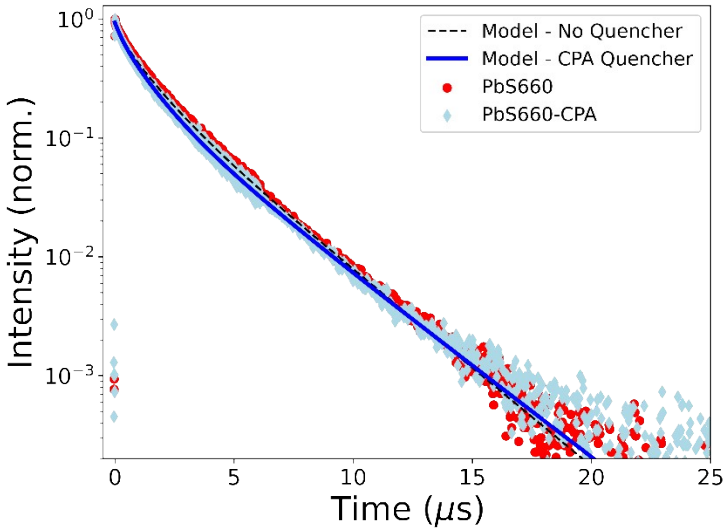

Figure S24. TRPL traces of PbS660 (red circles) and PbS660-CPA (pale blue diamonds) QDs integrated over the entire PbS emission spectrum, compared with our equilibrium model (solid blue line). From this QD ensemble we extract an equilibrium constant of K=0.3, consistent with more energetically favourable rTET compared to the ultrasmall QDs employed for upconversion photochemistry.

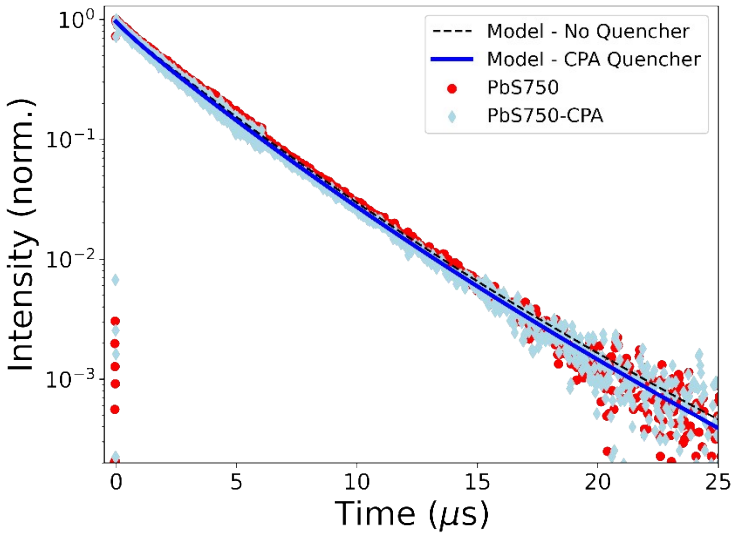

Figure S25. TRPL traces of PbS750 (red circles) and PbS750-CPA (pale blue diamonds) QDs integrated over the entire PbS emission spectrum, compared with our equilibrium model (solid blue line). From this QD ensemble we extract an even smaller equilibrium constant of K=0.1, consistent with more energetically favourable rTET compared to the ultrasmall QDs employed for upconversion photochemistry.

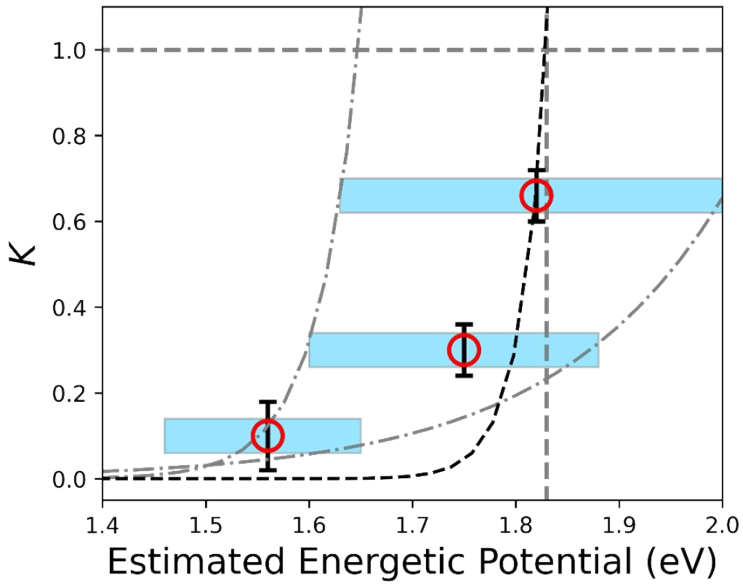

Figure S26. Extracted equilibrium constants (K) for TET as a function of the estimated energetic potential of ultrasmall PbS QDs. The shaded blue bars represent the energetic constraints provided by the absorption and emission energies of each QD ensemble, and the estimated potential is taken as the simple average. The dashed black line is a guide predicting the value of K from an energetic state around the anthracene triplet energy (1.83eV). The vertical dashed grey lines represent the anthracene triplet energy (1.83eV) and the horizontal dashed grey line corresponds to an equilibrium constant of K=1, intersecting where a hypothetical QD with energetic potential equal to 1.83 eV would have equal forward and reverse TET rate constants. We note that the shaded blue regions also represent the maximum Stokes' shift of these QDs, and the shift becomes progressively smaller as QDs become physically larger.

Light grey dot-dashed lines are exponential fits predicting the expected behaviour if the energetic potential arose solely from the emission spectrum (left side of blue bar) or absorption spectrum (right side of blue bar). We note that our data clearly falls in between these trends, though the guide (black dashed line) more closely resembles the behaviour of the peak emission energy. Error bars represent standard error estimated from our kinetic model for the fitted equilibrium constants.

References

(1) Green, P. B.; Narayanan, P.; Li, Z.; Sohn, P.; Imperiale, C. J.; Wilson, M. W. B. Controlling Cluster Intermediates Enables the Synthesis of Small PbS Nanocrystals with Narrow Ensemble Line Widths. *Chem. Mater.* **2020**, *32* (9), 4083–4094. https://doi.org/10.1021/acs.chemmater.0c00984.

(2) Li, X.; Huang, Z.; Zavala, R.; Tang, M. L. Distance-Dependent Triplet Energy Transfer between CdSe Nanocrystals and Surface Bound Anthracene. *J. Phys. Chem. Lett.* **2016**, *7* (11), 1955–1959. https://doi.org/10.1021/acs.jpclett.6b00761.

(3) de Mello, J. C.; Wittmann, H. F.; Friend, R. H. An Improved Experimental Determination of External Photoluminescence Quantum Efficiency. *Adv. Mater.* **1997**, *9* (3), 230–232. https://doi.org/10.1002/adma.19970090308.

(4) Ravetz, B. D.; Pun, A. B.; Churchill, E. M.; Congreve, D. N.; Rovis, T.; Campos, L. M. Photoredox Catalysis Using Infrared Light via Triplet Fusion Upconversion. *Nature* **2019**, *565*, 343–346. https://doi.org/10.1038/s41586-018-0835-2.

(5) Imperiale, C. J.; Green, P. B.; Miller, E. G.; Damrauer, N. H.; Wilson, M. W. B. Triplet-Fusion Upconversion Using a Rigid Tetracene Homodimer. *J. Phys. Chem. Lett.* **2019**, *10* (23), 7463–7469. https://doi.org/10.1021/acs.jpclett.9b03115.

(6) Li, X.; Nichols, V. M.; Zhou, D.; Lim, C.; Pau, G. S. H.; Bardeen, C. J.; Tang, M. L. Observation of Multiple, Identical Binding Sites in the Exchange of Carboxylic Acid Ligands with CdS Nanocrystals. *Nano Lett.* **2014**, *14* (6), 3382–3387. https://doi.org/10.1021/nl500885t.

(7) Piland, G. B.; Huang, Z.; Lee Tang, M.; Bardeen, C. J. Dynamics of Energy Transfer from CdSe Nanocrystals to Triplet States of Anthracene Ligand Molecules. *J. Phys. Chem. C* **2016**, *120* (11), 5883–5889. https://doi.org/10.1021/acs.jpcc.5b12021.

(8) Moreels, I.; Lambert, K.; Muynck, D. De; Vanhaecke, F.; Poelman, D.; Martins, J. C.; Allan, G.; Hens, Z. Size-Dependent Optical Properties of Colloidal {PbS} Quantum Dots. *ACS Nano* **2009**, *3* (10), 3023–3030. https://doi.org/10.1021/nn900863a.

(9) Wang, F.; Richards, V. N.; Shields, S. P.; Buhro, W. E. Kinetics and Mechanisms of Aggregative Nanocrystal Growth. *Chem. Mater.* **2014**, *26* (1), 5–21. https://doi.org/10.1021/cm402139r.

(10) Green, P. B.; Yarur Villanueva, F.; Imperiale, C. J.; Hasham, M.; Demmans, K. Z.; Burns, D. C.; Wilson, M. W. B. Directed Ligand Exchange on the Surface of PbS Nanocrystals: Implications for Incoherent Photon Conversion. *ACS Appl. Nano Mater.* **2021**, *4* (6), 5655–5664. https://doi.org/10.1021/acsanm.1c00853.

(11) Bender, J. A.; Raulerson, E. K.; Li, X.; Goldzak, T.; Xia, P.; Van Voorhis, T.; Tang, M. L.; Roberts, S. T. Surface States Mediate Triplet Energy Transfer in Nanocrystal-Acene Composite Systems. *J. Am. Chem. Soc.* **2018**, *140* (24), 7543–7553. https://doi.org/10.1021/jacs.8b01966.

(12) Chung, H.; Choi, H.; Kim, D.; Jeong, S.; Kim, J. Size Dependence of Excitation Energy Related Surface Trapping Dynamics in PbS Quantum Dots. *J. Phys. Chem. C* **2015**, *119* (13), 7517–7524. https://doi.org/10.1021/acs.jpcc.5b01810.

(13) Hinterding, S. O. M.; Vonk, S. J. W.; van Harten, E. J.; Rabouw, F. T. Dynamics of Intermittent Delayed Emission in Single CdSe/CdS Quantum Dots. *J. Phys. Chem. Lett.* **2020**, *11*, 4755–4761. https://doi.org/10.1021/acs.jpclett.0c01250.

(14) Hirayama, S. Effect of Substituent on the Behaviour of the Excited Singlet and Triplet States in Carbonyl Derivatives of Anthracene of the Type 9-X·CO·A. *J. Chem. Soc. Faraday Trans. 1 Phys. Chem. Condens. Phases* **1982**, *78* (8), 2411–2421. https://doi.org/10.1039/F19827802411.

(15) Han, Y.; He, S.; Luo, X.; Li, Y.; Chen, Z.; Kang, W.; Wang, X.; Wu, K. Triplet Sensitization by "Self-Trapped" Excitons of Nontoxic CuInS 2 Nanocrystals for Efficient Photon Upconversion. *J. Am. Chem. Soc.*

2019, *141* (33), 13033–13037. https://doi.org/10.1021/jacs.9b07033.